Environmental Science & Technology

pubs.acs.org/est

Article

Morphological, Microstructural, and In Situ Chemical Characteristics of Siderite Produced by Iron-Reducing Bacteria

Xiaohua Han,[&] Fuxian Wang,[&] Shiling Zheng, Hao Qiu, Yan Liu, Jian Wang, Nicolas Menguy, Eric Leroy, Julie Bourgon, Andreas Kappler, Fanghua Liu, Yongxin Pan, and Jinhua Li*

Cite This: *Environ. Sci. Technol.* 2024, 58, 11016−11026

Read Online

ACCESS | Metrics & More | Article Recommendations | Supporting Information

ABSTRACT: Dissimilatory iron-reducing bacteria (DIRB) oxidize organic matter or hydrogen and reduce ferric iron to form Fe(II)-bearing minerals, such as magnetite and siderite. However, compared with magnetite, which was extensively studied, the mineralization process and mechanisms of siderite remain unclear. Here, with the combination of advanced electron microscopy and synchrotron-based scanning transmission X-ray microscopy (STXM) approaches, we studied in detail the morphological, structural, and chemical features of biogenic siderite via a growth experiment with *Shewanella oneidensis* MR-4. Results showed that along with the growth of cells, Fe(II) ions were increasingly released into solution and reacted with CO_3^{2-} to form micrometer-sized siderite minerals with spindle, rod, peanut, dumbbell, and sphere shapes. They are composed of many single-crystal siderite plates that are fanned out from the center of the particles. Additionally, STXM revealed Fh and organic molecules inside siderite. This suggests that the siderite crystals might assemble around a Fh-organic molecule core and then continue to grow radially. This study illustrates the biomineralization and assembly of siderite by a successive multistep growth process induced by DIRB, also provides evidences that the distinctive shapes and the presence of organic molecules inside might be morphological and chemical features for biogenic siderite.

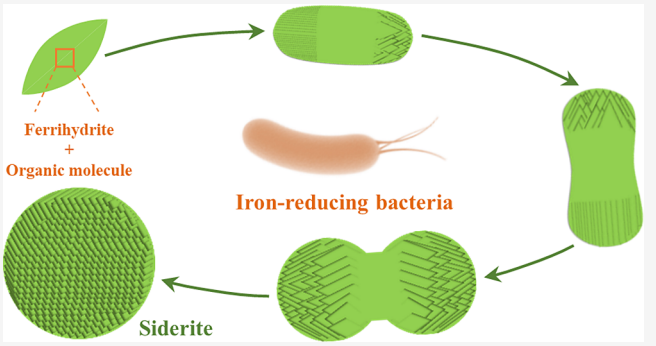

KEYWORDS: *siderite, dissimilatory iron reduction, Fh-organic molecule core, HRTEM, STXM-NEXAFS*

INTRODUCTION

Dissimilatory iron-reducing bacteria (DIRB) are ubiquitous and important for the fate of metals and organic matter in diverse natural environments.[1,2] These organisms have the capability of using ferric ions as electron acceptors and organic compounds or H_2 as electron donors to produce dissolved ferrous ions, which often result in the extracellular formation of ferrous minerals (e.g., siderite ($FeCO_3$) and vivianite ($Fe_3(PO_4)_2{\cdot}8H_2O$)) or mixed-valence iron minerals (e.g., magnetite (Fe_3O_4) and green rust ($[Fe(II)_{1-x}Fe(III)_x(OH)_2]^{x+}{\cdot}[(x/n)A^{n-}, mH_2O]^{x-}$)).[3−5] Such mineralization processes induced extracellularly by DIRB could affect directly and indirectly the redox cycling and mobilization of metals and the degradation of organic contaminants in modern groundwater, soil, and sediment systems.[6,7]

Unlike size-tailored and morphology-controlled magnetite nanocrystals biologically controlled by magnetotactic bacteria,[8,9] both the mineralization process and products extracellularly induced by DIRB can be influenced significantly by environmental factors under which the bacteria are growing.[10−12] For instance, DIRB produced magnetite, a mixed-valence and ferromagnetic magnetic mineral, as major end products when the bacteria are growing anaerobically with ferrihydrite (Fh) as a ferric source and HEPES (4-(2-hydroxyethyl)-1-piperazine-ethanesulfonic acid) or PIPES (1,4-pipera-zinediethanesulfonic acid) as a buffer.[3,11] Generally, DIRB produces nanometer-sized magnetite aggregates that are typically superparamagnetic via a solid-state conversion of poorly crystalline Fe(III) (oxyhydr)oxides.[12−14] Larger and well-crystallized magnetite particles that are single domain magnetic could also be formed by some DIRB strains or when they are growing for a long time or in a high-temperature environment.[15,16]

Besides nanometer-sized magnetite, siderite and vivianite could be induced as major end products when the bacteria are growing in a bicarbonate-buffered solution without or with phosphorus.[3,17] Vivianite with bladed and fibrous morphologies were observed when the Fe(II) concentration was high enough to combine with PO_4^{3-} in an aqueous solution.[18] By

Received: December 29, 2023
Revised: April 29, 2024
Accepted: April 30, 2024
Published: May 14, 2024

contrast, siderite produced by DIRB has various shapes, e.g., rod, cubic, disk-like, dumbbell, sphere, and rhombohedral.[3,11,19−21] However, the mineralization process and mechanisms of siderite precipitation into these different morphologies induced by DIRB are in a long-standing controversy. Dong et al. found that magnetite could be used as a Fe(III)-containing reduction substrate by *Shewanella putrefaciens* for the formation of siderite, i.e., magnetite could be a precursor for siderite.[22] In contrast, Zachara and coworkers documented that higher [HCO_3^-] in the medium could inhibit the formation of magnetite but accelerate the nucleation of siderite.[23] On the other hand, abiotic experiments showed that the precipitation of siderite could be initiated by the nucleation of amorphous iron carbonates and subsequently accelerated by an outer ring growth of crystalline phases.[24,25] This indicates that the biogenic siderites might be different in both mineralogy and morphology from their abiotic counterparts but also be dependent on the Fe(III)-containing reduction substrate and chemical environment in the medium in which the bacteria are growing.

To investigate the biomineralization process and mechanisms of siderite extracellularly induced by DIRB, we performed a time-course growth experiment with *Shewanella oneidensis* MR-4 with Fh as the ferric source in a bicarbonate buffer. A combination of Raman imaging and scanning electron microscopy (RI-SEM), scanning electron microscopy (SEM), transmission electron microscopy (TEM), X-ray diffraction (XRD), synchrotron-based scanning transmission X-ray microscopy (STXM), and rock magnetism approaches was used to monitor and characterize the formation and variation of both magnetite and siderite in the solution for 54 days. Finally, a biomineralization model of siderite extracellularly induced by strain MR-4 was tentatively proposed.

MATERIALS AND METHODS

Strains and Medium. *S. oneidensis* MR-4 used in this study was isolated originally from the Black Sea.[26] Detail information about the medium is provided in the Supporting Information.

Preparation of Fh Substrates and Incubation Experiments. Fh was prepared by the reaction of $FeCl_3{\cdot}6H_2O$ (1 M) with NaOH (1 M) until pH 7.0.[5] The Fh was centrifuged (4293 × *g*; 10 min) and washed three times with ultrapure H_2O (18 MΩ deionized water, Milli-Q), and it was finally kept in suspension. For mineralization experiments, the medium contained the following (per liter): 2.5 g of $NaHCO_3$, 0.6 g of $NaH_2PO_4{\cdot}H_2O$, 0.25 g of NH_4Cl, and 0.1 g of KCl, as well as 10 mL of Wolfe's vitamin and 10 mL of trace element solutions. The sterilized medium was added by 25 mM Fh and 30 mM lactate, adjusted pH to ∼7.8 with 1 M HCl, and then transferred into 1 L serum bottles which were crimp-sealed (each bottle contained 500 mL of the mineralization medium). Before inoculation, the headspace in each serum bottle was flushed with N_2:CO_2 (v:v, 80%:20%) for 1 h. Triplicate bottles were used for biotic experiments, and each bottle was inoculated with 6 mL of the precultured MR-4 cells and incubated at 30 °C in the dark. Triplicate bottles were sampled at intervals of 0, 1, 3, 7, 9, 11, 14, 17, 20, 23, 26, 32, 38, 40, 44, 48, and 54 days for protein concentration, Fe concentration, pH quantification, TEM and SEM-Raman experiments.

Protein Concentration, Fe Concentration, and pH Quantification. We used the protein concentration (μg/mL) over time to monitor bacterial growth because the aggregates of cells and minerals made the counting of cells difficult.[27] For protein concentration analyses, 2 mL of culture slurry was centrifuged at 12,045 × *g* for 5 min, and the solid pellets were resuspended in 300 μL of 0.1 M NaOH and heated at 90 °C for 15 min. Afterward, the samples were centrifuged at 4293 × *g* for 20 min. Ten μL supernatants were mixed with 190 μL of BCA Protein Assay Kit (Thermo Fisher Scientific) and heated at 37 °C for 30 min. Finally, the protein concentrations of cultures were measured by the spectrophotometer at OD_{562} (optical density at 562 nm). For the Fe concentration, 1 mL of culture slurry was centrifuged at 12,045 × *g* for 5 min. The supernatant was mixed with anoxic 1 M HCl to prevent Fe(II) oxidation, and solid pellets were dissolved in anoxic 1 mL of 6 M HCl for 24 h and then diluted in anoxic 1 M HCl. Both Fe(II) and total Fe concentrations in the aqueous phases and solid phases were quantified by the spectrophotometric ferrozine assay, and Fe^{3+} concentrations in precipitates were calculated as the difference between Fe(total) and Fe^{2+}.[28] Two mL of culture slurry was used for pH analysis by a DELTA320 pH meter. All sampling processes for protein concentration, Fe concentration, pH quantification, and separation processes for Fe concentration were carried out in an anoxic glovebox (100% N_2). Sample separation processes for protein concentration and pH quantification were conducted under oxic conditions.

Microscopic Experiments. The samples for microscopic experiments were sampled, centrifuged (12,045 × *g*, 5 min), and dried in an anoxic glovebox (100% N_2). The dried samples were mounted onto the surface of glass slides for SEM and RI-SEM analyses, carbon-coated copper grids for TEM analyses, and silicon nitride windows for synchrotron-based STXM analyses.[29] The RI-SEM system consists of a Zeiss (Germany) field scanning electron microscope (Gemini 450) with an acceleration voltage range of 0.02−30 kV and a highly sensitive WITec (alpha 300R, Germany) confocal Raman microscope.[30] Microchemical analyses were made by SEM with energy-dispersive X-ray spectrometry (EDXS). In situ focused ion beam (FIB)-milling sample preparation for TEM was performed with a Zeiss Auriga Compact dual beam FIB-SEM system.[31] TEM observations were performed on a JEOL JEM-2100HR TEM and a JEOL JEM-2100F TEM at 200 kV. The crystal orientation of mineral products was determined with an ASTAR system, which is an automatic crystal orientation mapping (ACOM) system installed on a FEI Tecnai F20 microscope.[32] The ACOM experiments were acquired with a 0.5° precession angle in order to minimize the dynamical effects in the diffraction patterns.

Synchrotron-based STXM experiments were carried out at the 10ID-1 Soft X-ray Spectromicroscopy (SM) Beamline at the Canadian Light Source (CLS).[33] X-ray absorption spectroscopy (XAS) images were generated by x-y raster scanning while recording the intensity of transmitted X-rays. A sequence of XAS images, which covers the energy region of interest (e.g., 280−320 eV for C 1s, 525−560 eV for O 1s, and 700−730 eV for Fe 2p), was recorded for spectroscopic analysis. The measured transmitted signals (I) were converted to optical density (i.e., absorbance, OD = $-\ln(I/I_0)$) using the incident flux (I_0) measured in the absence of the sample. All processing was performed using aXis2000 (http://unicorn.mcmaster.ca/aXis2000.html).

Magnetic and XRD Experiments. Methods and results of magnetic and XRD experiments for final mineral products collected at day 54 are provided in the Supporting Information. Figure S1 shows the typical magnetic characteristics of

https://doi.org/10.1021/acs.est.3c10988
Environ. Sci. Technol. 2024, 58, 11016−11026

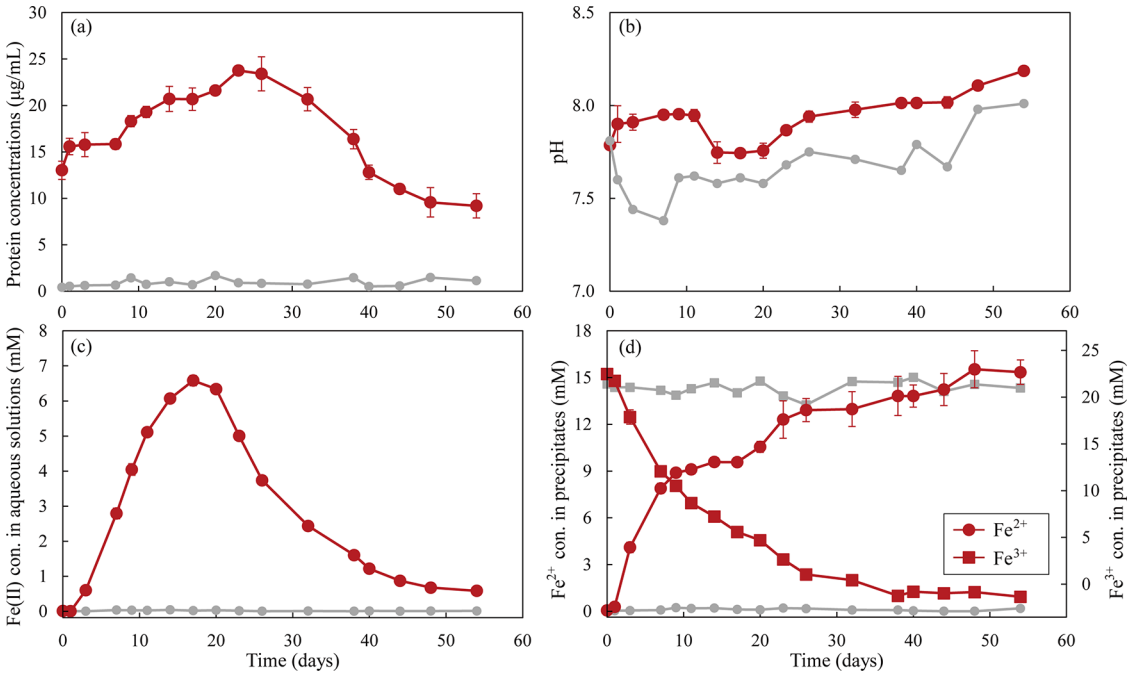

Figure 1. Protein concentration (a), pH (b), Fe(II) concentration in aqueous solution (c), and Fe^{2+} and Fe^{3+} concentration in precipitates (d) during ferrihydrite reduction catalyzed by *S. oneidensis* MR-4. Red and gray symbols and lines refer to biotic experiments and abiotic control, respectively. Fe^{3+} concentrations in precipitates were calculated as the difference between Fe(total) and Fe^{2+}. Error bars that are not visible are smaller than the symbols.

magnetite and siderite.[14,34,35] Figure S2 shows the typical mineral characteristics of siderite.

RESULTS

Bacterial Growth, Fe(II) Release, and Mineral Transformation. As shown in Figure 1a, the protein concentrations increased gradually from ~13 to ~24 μg/mL within the first 23 days of incubation and then declined to ~9 μg/mL within 54 days (Table S1). The protein concentration curve did not reflect the exponential growth of cell density in the time course, although the previous study has shown that the protein content was well correlated to the dry cell weight which indicated that protein quantification was a suitable method for indirect biomass estimation.[27] Protein content could be different from cell counts due to the variations in cell size and protein content over the growth phase. At the beginning of experiments, when a lot of substrate was available, the cells might have been bigger and had more protein than in the late exponential growth phase. The pH of the biotic experiments increased from ~7.8 to ~8.2, but it showed no obvious differences compared to the control bottle without bacteria (Figure 1b). The concentration of Fe(II) in aqueous solutions increased from near zero to 6.58 mM within the first 17 days and then decreased to near zero (0.58 mM) after 54 days (Figure 1c), while no water-soluble Fe(III) was detected in the aqueous solution. The Fe^{2+} in the precipitates increased from near zero to 15.34 mM, and Fe^{3+} in the precipitates decreased from 22.47 mM to near zero along with Fe(III) reduction by MR-4 (Figure 1d). Since there were mainly Fe(II)-bearing minerals (siderite) in precipitates after 40 days, Fe^{2+} concentrations and total Fe concentrations were very close. Therefore, Fe^{3+} concentrations calculated as the difference between Fe(total) and Fe^{2+} showed slightly negative values at some time points due to the low precision of the spectrophotometric ferrozine assay and the low amount of Fe^{3+}. Although the initial total Fe concentration in incubation bottles was ~22 mM, the final total Fe concentration was ~16 mM. This mass unbalance could be due to the precipitation/sorption of Fe to the glass wall of incubation bottles. Similar precipitation/sorption was detected by adding phenanthroline to an emptied glass bottle which immediately revealed the presence of Fe in Notini et al.[36]

The formation of magnetite and siderite was observed by electron microscopy. SEM, RI-SEM, and TEM analyses showed that magnetite was formed first and then siderite (Figures S3 and 2). Conventional TEM and high-resolution TEM (HRTEM) of samples collected after 3 and 14 days showed that magnetite was formed (Figure S3). The magnetite generally occurred as loose aggregates with nanoparticles, similar to those magnetite products produced by other DIRB strains in previous studies.[12,37] Even when siderite formed, ~5.6 mM Fe^{3+} was still left in the precipitates on day 17. Additionally, we also observed ferrihydrite by SEM-Raman on day 17. Therefore, it is possible that there was still magnetite precipitated after day 17. Until 54 days, magnetite nanoparticles could still be found by TEM (Figure S3), although the mineral phase of magnetite and Fe^{3+} in precipitates on day 54 was undetectable by XRD (Figure S2) and spectrophotometric ferrozine assay (Figure 1d) due to the extremely low amount of magnetite.

Distinct from irregular shapes of magnetite and Fh, micrometer-sized siderite particles with spindle, rod, peanut, dumbbell, and sphere shapes were observed from day 17 to day 54 (Figure 2a–j). The siderite probably grew in progressive stages involving a morphological transition from spindle to rod, to peanut, to dumbbell, and to spherical shape (Figure 2), as described in the synthesis of siderite microspheres using a biomolecule-assisted hydrothermal strategy.[38] This growth should start from the spindle-shaped siderite with two pointed

https://doi.org/10.1021/acs.est.3c10988
Environ. Sci. Technol. 2024, 58, 11016−11026

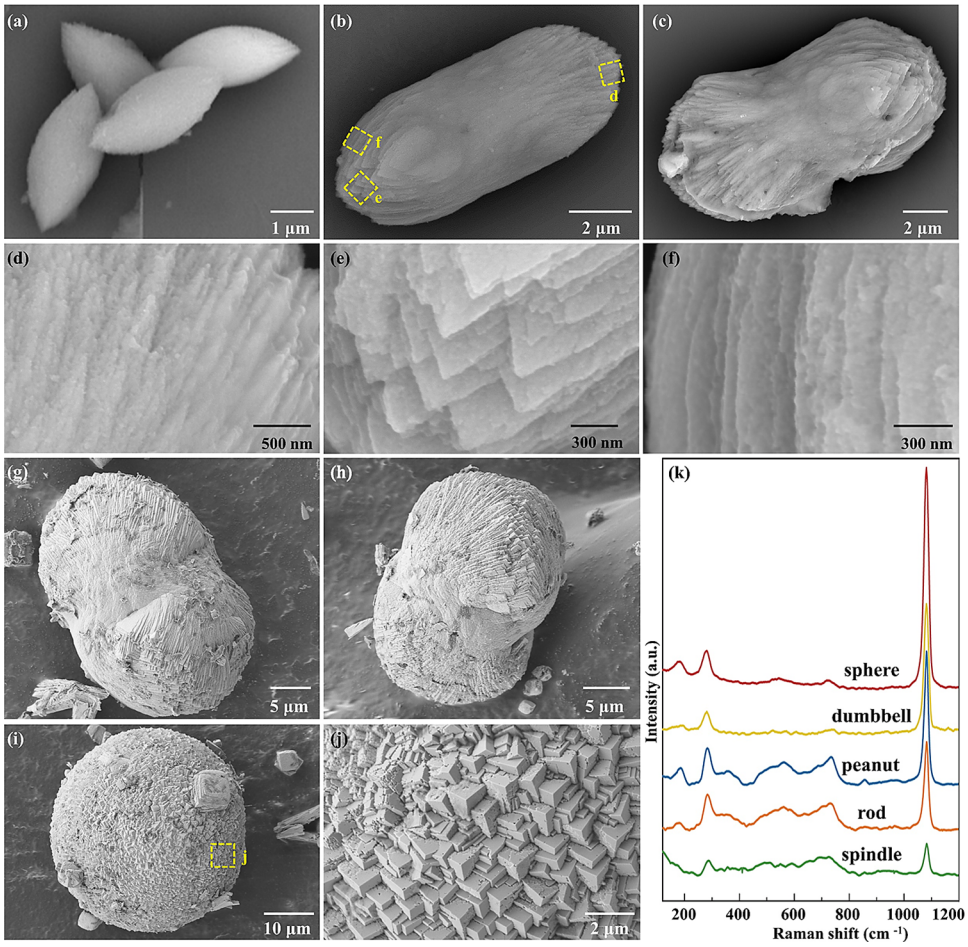

Figure 2. SEM micrographs (a–j) and Raman spectra (k) of siderite produced by *S. oneidensis* MR-4, showing different shapes: spindle (a), rod (b), peanut (c), dumbbell (g, h), and sphere (i). (d), (e), (f), and (j) are close-up images of rod and sphere siderite particles. Additional SEM-EDXS elemental mapping of Fe, O, and C for siderite particles is shown in Figure S5.

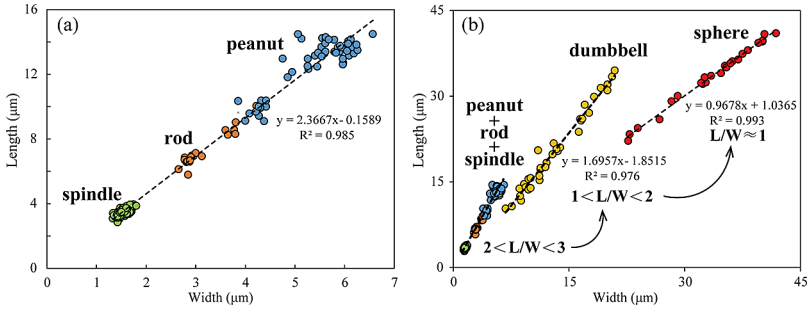

Figure 3. (a, b) Length versus width variations of different siderite morphotypes: spindle (green), rod (orange), peanut (blue), dumbbell (yellow), and sphere (red). The dashed line in each panel marks a linear regression between the length and width of each shaped siderite product. Details of the size distribution for siderite products with different morphotypes are shown in Figure S6.

ends and a wider middle section (Figure 2a). With growth at both ends, siderites form rod- and peanut-shaped particles (Figure 2b,c). High-magnification SEM imaging shows that both the rod-shaped and peanut-shaped siderites are composed of many nanometer-thick siderite plates, which are stacked on top of each other (Figures 2d–f and S4). Followed by self-similar fanning out from the center, siderites gradually become dumbbell-shaped (Figure 2g,h) and end up with a symmetrical spherular shape (Figure 2i,j). Raman spectra have helped to identify the siderite with various shapes by its bands around 1083, 287, 184, and 731 cm^{-1} (Figure 2k). All of the peaks are strong and sharp, indicating that the siderite particles are well crystallized. The three small peaks/shoulders at 330, 560, and 685 cm^{-1} are the characteristics of magnetite that might stick on the surface of siderite. However, these magnetite nanoparticles are too small to be readily detected by SEM imaging.

As shown in Figure S6, a total of 223 siderite particles were used to observe their morphology and size distribution, which all fell into each category (spindle, rod, peanut, dumbbell, and sphere shapes). Since the nucleation and growth of siderite occurred simultaneously, siderite with different morphologies were observed at the same time point. However, spindle-, rod-,

https://doi.org/10.1021/acs.est.3c10988
Environ. Sci. Technol. 2024, 58, 11016–11026

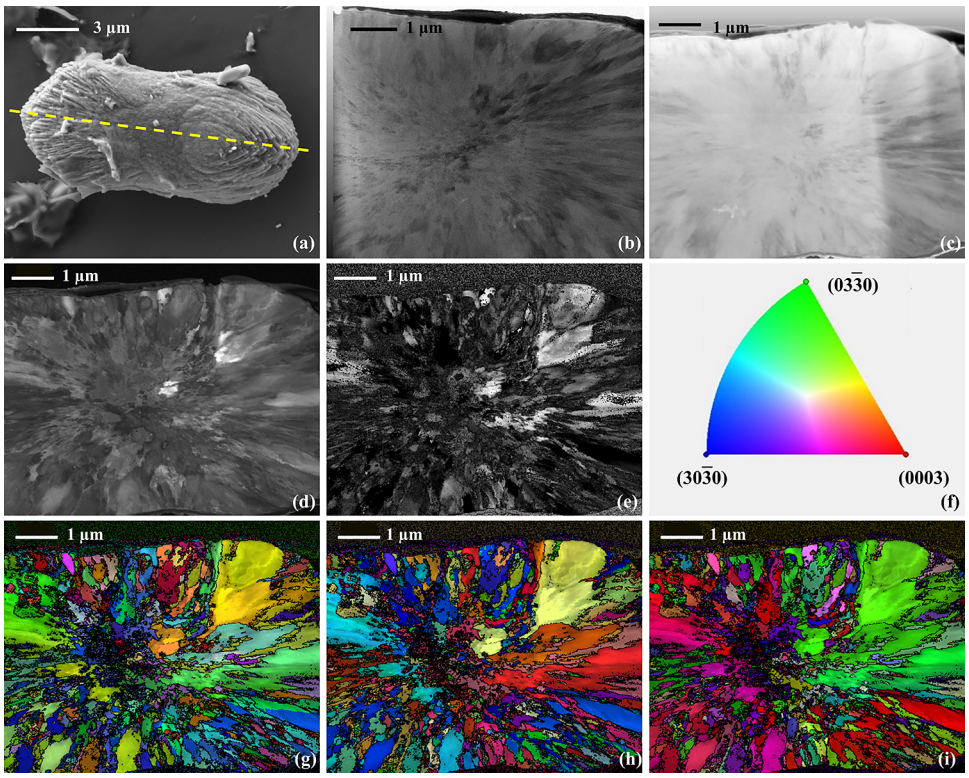

Figure 4. Crystal orientation of siderite produced by *S. oneidensis* MR-4. The yellow line in (a) refers to an FIB cross-section that was cut along the long side of the siderite particle. (b) is the TEM image of the central part of the FIB cross-section. (c–i) ACOM orientation mapping of siderite. (c) Virtual bright field map, (d) correlation index map, (e) reliability index map, (f) color key, (g) *x* orientation map, (h) *y* orientation map, and (i) *z* orientation map. Precession angle: 0.5°, frequency: 100 Hz, beam spot size: 1.5 nm, scanning step size: 15 nm, condenser aperture: 50 μm, camera length: 89 mm.

and peanut-shaped siderites were mainly observed from day 17 to day 38, while dumbbell- and sphere-shaped siderites were mainly observed from day 40 to day 54. Along with the morphological transition from spindle to sphere shape, both the length and width of siderite particles increase and eventually grow into the same values (Figure 3). To quantitatively characterize the morphotype transition, shape factors (length divided by width, L/W) are used here to describe the relative variations of the length and width of siderite particles. For instance, the length of siderites increased from ∼3−4 μm in spindle-shaped particles to ∼6−10 μm in the rods, and then to ∼9−15 μm in peanut-shaped minerals (Figure 3a). Although the shapes are different, all L/W values of spindle-, rod-, and peanut-shaped siderites are between 2 and 3. L/W values of dumbbell-shaped siderites were between 1 and 2 with a length of ∼10−35 μm and width of ∼6−22 μm, indicating there was faster growth in width relative to length when the shape shifted to the dumbbell-shaped structures (Figure 3b). This compensated for growing faster in length than in width in the early stages of siderite formation (spindle, rod, and peanut) and contributed to the final formation of sphere-shaped siderite. As for the driving forces for the formation of spherical minerals, the previous hypothesis involved Brownian motion, magnetic attraction, electric dipolar interaction, or other physical or energetic processes.[39−41] Finally, L/W values were close to 1 when siderites formed in spherical shape, which had diameters ranging from ∼20 to ∼45 μm (Figure 3b). Additionally, for the dumbbells and the spheres if they have the same width, the spheres could grow from dumbbells smaller than that, while the dumbbells could grow to spheres bigger than that. The siderite crystal growth proceeded as a miniature rhombohedral siderite (∼2 μm in edge length; Figure 2i) on the surface of the spherical siderite.

Structural and Chemical Features of Siderite. In order to explore the internal structure of the siderite with TEM and synchrotron-based STXM approaches, we made FIB foils from the center and along the long axis of the particle (yellow line in Figure 4a). TEM observations clearly showed that the siderite crystals radiate outward from the center (Figure 4b). Additionally, a SEM image of a broken spherulite (Figure S7) reveals the solid internal structure of the siderite spherulite, exhibiting a radial growth pattern. It appears that the siderite spherulites are formed by the process of subunit aggregation. Automatic crystal orientation mapping (ACOM) showed that the center part of the siderite particle appears to be less crystalline and relatively homogeneous in texture. The center part is distinctive from these siderite fibers, which radially distribute around it. The mineral phase of siderite is confirmed by the correlation index map in which crystals appear as white to light gray pixels (Figure 4c,d), except for the black to light gray pixels, which are likely due to thickness variations (Figure 4e). The *x*, *y*, and *z* orientation maps (multiplied by the index map) indicate that the siderite particles have no privileged growth axis and grow radially (Figure 4g–i).

Despite the textural difference, TEM-EDXS elemental mapping showed no obvious chemical difference between the center part and the other regions inside siderite. Iron, oxygen, and carbon elements are uniformly distributed inside of siderite as shown in Figure 5b–d. However, synchrotron-based

https://doi.org/10.1021/acs.est.3c10988
Environ. Sci. Technol. 2024, 58, 11016−11026

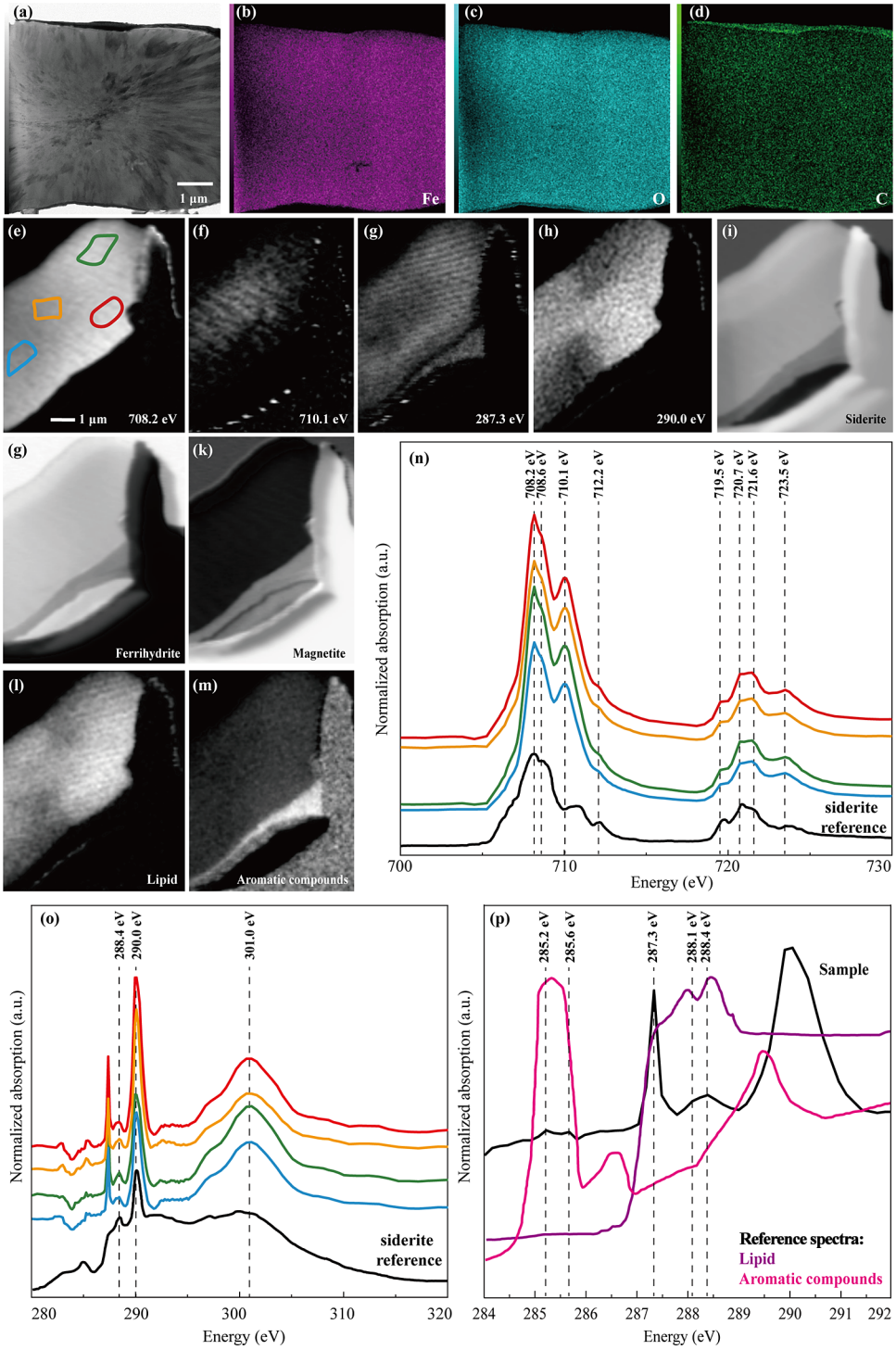

Figure 5. TEM-EDXS elemental mapping and synchrotron-based STXM analysis for an FIB cross-section of the siderite produced by *S. oneidensis* MR-4. (a–d) TEM-EDXS elemental mapping shows the spatial distribution of iron (purple), oxygen (blue), and carbon (green). (e–h) STXM images of Fe L-edge (708.2 and 710.1 eV) and C K-edge (287.3 and 290.0 eV). (i–m) Component maps of (i) siderite, (g) ferrihydrite, (k) magnetite, (l) lipid, and (m) aromatic compounds derived by fitting reference spectra. Fe L-edge (n) and C K-edge (o) NEXAFS spectra of four different positions (red, yellow, blue, and green areas) marked accordingly in the FIB cross-section (e) compared with references siderite (black lines). (p) Comparison of C K-edge NEXAFS spectra of siderite (black line) and reference organic matter of lipid (purple line) and aromatic compounds (pink line).

STXM analysis on the FIB cross-section of the siderite particle showed a heterogeneous distribution of chemical components (Figure 5e–h). Near edge X-ray absorption fine structure (NEXAFS) at the Fe $L_{2,3}$-edge (2p1/2,3/2 → 3d) is sensitive to the speciation of Fe, including its redox state.[42] The NEXAFS spectra at the Fe $L_{2,3}$-edge measured on four different positions of the FIB cross-section show the characteristic of siderite (Figure 5n: a stronger double-peak at 708.2/708.6 eV and a weaker peak at 710.1 eV for Fe L_3-edge; three peaks at 719.5 eV, 720.7 eV and 723.5 eV for Fe L_2-edge).[43] The

https://doi.org/10.1021/acs.est.3c10988
Environ. Sci. Technol. 2024, 58, 11016–11026

singular value decomposition (SVD) analysis using reference NEXAFS spectra further confirms the presence of siderites (Figure 5i).[44] Additionally, the obvious peak at 710.1 eV on four different positions of the FIB cross-section indicates that Fe^{3+} is present inside the siderite. The SVD analysis shows that the Fe^{3+}-containing species should be Fh (not magnetite), which was encased during siderite nucleation and growth (Figure 5g,k). However, selected area electron diffraction (SAED) patterns of several areas on the FIB cross-section only showed a typical pattern for siderite (Figure S8), and the distinct reflections of Fh have not been observed due to its low amount and crystallinity. Because of the low amount, the spectrophotometric ferrozine assay also failed to detect the presence of Fh.

The NEXAFS spectra at the C K-edge showed the characteristic of CO_3^{2-} in siderite (Figure 5o): a strong peak at 290.0 eV, a well-defined pre-edge peak at 288.4 eV, and a broad peak at 301.0 eV, which are consistent with that reported in Brandes et al.[45] Except for the carbonate, STXM analysis performed at the C K-edge showed the presence of organic functional groups typically associated with microorganisms (Figure 5p). The sharp peak at 287.3 eV and the flat shoulder at 288.1 eV are related to 1s → 3p/s* electronic transitions of carbon in hydrocarbon functional groups (C−H), which are associated with aliphatic compounds. The flat peak at 288.4 eV is attributed to 1s → π^* electronic transitions of carbon in the carboxyl group (−COOH). These results indicate a higher aliphatic compounds content within the precipitated siderite, probably stemming from the phospholipid bilayer of the cells. Based on the SVD analysis using reference NEXAFS spectra, lipids match clearly with the FIB cross-section of siderite (Figure 5l). The two flat peaks at 285.2 and 285.6 eV correspond to the electronic transition of carbon in aromatic carbon groups (C═C).[46,47] The signal of these groups was relatively lower inside the siderite, as identified by SVD analysis shown in Figure 5m.

In NEXAFS spectra at the O K-edge (Figure S9), the first intense and sharp peak at 534.2 eV is assigned to the π^* antibonding state from the C═O bonds of CO_3^{2-} resulting from out-of-plane π bonds involving only p states. The two higher energy peaks at 539.6 and 543.0 eV of the spectrum correspond to the σ^* antibonding state of CO_3^{2-}.

DISCUSSION

Biomineralization of Magnetite and Siderite during Iron Reduction by MR-4. Magnetite and siderite are the frequently observed products from Fe(III) (oxyhydr)oxide (e.g., ferrihydrite) reduction by DIRB, but the formation sequence of magnetite and siderite during DIRB reduction is controversial. Thermodynamic calculations for hydrous ferric oxide reduction by *Shewanella putrefaciens* CN32 in a bicarbonate-buffered medium suggested that the magnetite stability field would be encountered before that of siderite.[3] Additionally, laboratory results of siderite formation from biogenic and abiotic magnetite by *S. putrefaciens* strains CN32 and MR-1 also supported that magnetite could be a precursor for siderite formation.[22] However, Zachara et al. have observed that biomineralization products were almost identical in both MES [2-(*N*-morpholino)ethanesulfonic acid] and bicarbonate buffers where Fh was reduced by *S. putrefaciens* CN32 as a function of N_2:CO_2 ratio (100:0−80:20).[23] They have found that both of these buffer systems were in equilibrium with CO_2 and contained equivalent bicarbonate concentrations at the same pH based on model calculations and chemical analyses, indicating that the formation of siderite did not proceed through a magnetite intermediate. Instead, they have proposed another mechanism for the sequence of magnetite and siderite precipitation in which higher HCO_3^- concentrations appeared to prevent topotactic conversion to magnetite through aqueous complexation of Fe(II) or surface complexation of HCO_3^- that inhibited magnetite formation and/or accelerated nucleation of siderite. Table S2 summarizes the incubation conditions for DIRB experiments in which siderite and magnetite are coexisting products. Based on the summarized results, the most important factor for siderite formation is the presence of HCO_3^- and/or CO_3^- in the incubation system.

There was a slight increase of pH from ∼7.8 to 8.2 in the biotic experiments and the control bottle which could have resulted from a gradual desorption of OH^- from the surface of Fh substrates with time.[48] Considering the $FeCO_3$ solubility product (K_{sp}) of $10^{-10.93}$,[49] and the sum of HCO_3^- and CO_3^{2-} concentrations being 30 mM here, $FeCO_3$ is expected to precipitate when the Fe(II) concentration is higher than $3.3 \times 10^{-3.93}$ mM. However, there was no siderite observed in the first 14 days in which the Fe(II) concentration was as high as 6 mM. One possible interpretation is that the solubility of magnetite ($10^{-108.18}$) was much smaller than that of siderite at room temperature.[50] Additionally, no siderite precipitated in abiotic control experiments in which 6.58 mM Fe(II) was added to a 30 mM $NaHCO_3$ solution (pH 7.8). Previous studies suggested that in the absence of a nucleation site or suitable surface, siderite precipitates via homogeneous nucleation, where solution saturation has to surpass a critical threshold that is significantly higher than siderite equilibrium solubility.[25,51] Here in our study, the Fe L-edge and C K-edge NEXAFS spectra showed the presence of Fh and organic molecules inside siderite particles, which could have provided a nucleation site to allow the crossing of the nucleation barrier and subsequent siderite formation. Similarly, previous studies demonstrated that siderite crystals could nucleate on bacterial nanoglobules as for Ca- and/or Mg-carbonate precipitation.[52,53] The outer membrane of iron(III)-reducing bacteria and their exopolysaccharides (EPS) could bind metal ions and serve as nucleation sites for siderite formation.[21,54] Additionally, these results suggest that magnetite does not need to be a necessary precursor for siderite during DIRB mineralization.

Although various shapes (e.g., rod, cubic, disk-like, dumbbell, sphere, and rhombohedral) of siderite were reported during bacterial iron(III) reduction,[3,11,19,20,21] spindle- and peanut-shaped siderite particles produced by DIRB were first reported in the present study. The morphological evolution of the biogenic siderite particles involves a spindle-rod-peanut-dumbbell-sphere transition. Additionally, we have observed obvious differences in growth rates between the length and width of siderite particles. The spindle-, rod-, and peanut-shaped siderites ($2 < L/W < 3$) exhibit a relatively faster growth in length, while dumbbell-shaped siderites ($1 < L/W < 2$) show a relatively faster growth in width. Qu et al. have captured a similar growth pattern by slowing down the reaction rate of biomolecule ascorbic acid (vitamin C)-assisted hydrothermal synthesis of siderite in lower-temperature experiments.[38] They suggested that the intrinsic electrical dipole interactions between the assembled subunits are responsible for the aggregation of the siderite subunits. In addition to the work by Qu et al., other studies have proved that organic molecules (e.g., ascorbic acid and poly(ethylene

https://doi.org/10.1021/acs.est.3c10988
Environ. Sci. Technol. 2024, 58, 11016−11026

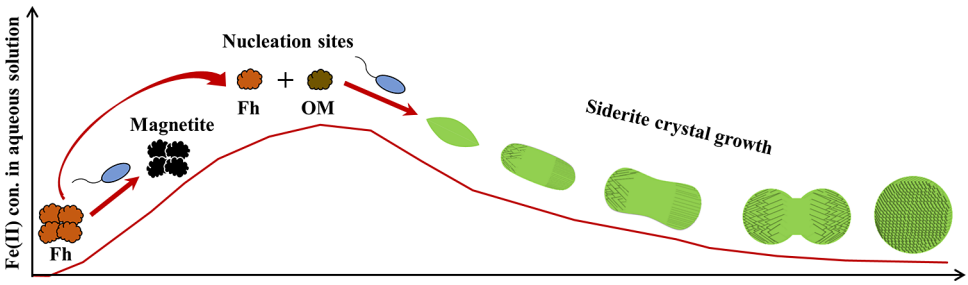

Figure 6. Overview of biomineralization of magnetite and siderite during iron reduction by *S. oneidensis* MR-4. The red line refers to the Fe(II) concentration in an aqueous solution. Fe(II) produced by reduction of Fh by *S. oneidensis* MR-4 was low in the beginning of the reduction experiments and reacted with Fh immediately, resulting in magnetite formation. Along with the growth of cells, more Fe(II) was produced and combined with CO_3^{2-} in aqueous solutions, then forming siderite with Fh and organic molecule as nucleation sites and growing into larger particles following the spindle-rod-peanut-dumbbell-sphere transition.

glycol)-*block*-poly(methacrylic acid)) can contribute to the multistep aggregation of subunits and control the crystal orientation, morphology and polymorph selection of carbonate minerals.[55,56] For instance, the π-bond conjugation due to the two hydroxyl groups (−OH) of the ascorbic acid molecule could dissociate protons or produce interactions with electropositive carriers, thus the ascorbic acid could further interact with the positively charged faces of siderite during the reaction.[38] In our study, NEXAFS spectra at the C K-edge showed the presence of carboxyl groups (−COOH) inside siderite, which could also exert a similar influence on the assembly of the subunits and siderite growth via electrostatic attraction like that of ascorbic acid. Overall, our study highlights the significant role of organic molecules in the multistep mineralization process of siderite and provides deeper insights into the formation of biogenic minerals assembled by subunits.

Combing with the Fe(II) concentration in the aqueous solution and mineralogy results in this study, we suggest that the rate and concentration of Fe(II) flux dominated the secondary mineralization products of DIRB. A growth model of magnetite and siderite during iron(III) mineral (ferrihydrite) reduction by *S. oneidensis* MR-4 is shown in Figure 6. The Fe(II) produced from reduction of Fh reacted with Fh immediately at the beginning of experiments, resulting in magnetite formation via a solid-state conversion of Fh.[57] Along with the growth of cells, more Fe(II) was produced and released into solution, thus being available to react with CO_3^{2-} and form siderite with Fh and organic molecules functioning as nucleation sites. The whole biomineralization process of siderite follows the successive multistep growth process which involves a spindle-rod-peanut-dumbbell-sphere morphological transition.

Environmental Implications. Siderite has been frequently described as an Fe(II)-carbonate precipitate in soils and sediments. Its formation was generally associated with bacterial respiration of organic matter coupled to microbial Fe(III) mineral reduction, which has a strong influence on the biogeochemical cycling of Fe and C throughout much of Earth's history.[58] Our study has shown that the Fe(III) substrate (e.g., ferrihydrite), bacterial cells, and associated biomass could function as nucleation sites for siderite formation, making it easier for siderite to cross the nucleation barriers and subsequent forming. Given the abundance of Fe(III) (oxyhydr)oxide minerals and Fe(III)-reducing bacteria in anoxic sedimentary systems, biogenic siderite precipitation could preserve carbon inside the minerals and prevent degradation.

Additionally, the spindle-, rod-, peanut-, and dumbbell-shaped siderite particles with radial subcrystals had not previously been found in abiotic experiments in the absence of organic matter. These distinct shapes and structures might therefore be features of biogenic siderite, which is very important for the identification of biogenic siderite in the ancient (and modern) geological record on Earth. Previous studies have found the micron- to submicron-scale rod-, peanut-, and dumbbell-shaped siderite crystals comprising of radial subcrystals in Otter Lake sediments older than ∼1200 years BP (years before present) and windward lagoon core from Bora Bora deposited around 7700 years BP.[59,60] In particular, these siderite crystals found in sediments are mostly identical in shape and size to those formed in our study. Nanometer-sized siderite likely related to microbial mediation has been observed in the Rio Tinto basin, which is an acid-sulfate condition regarded as an analogue for early Earth.[21] Future studies on morphological characteristics and microscopic chemical compositions of the siderite in the sediments using advanced electron microscopy and scanning transmission X-ray microscopy will provide more definitive evidence for the abiotic or biotic origin of siderite in sediments on Earth.

■ ASSOCIATED CONTENT

Supporting Information

The Supporting Information is available free of charge at https://pubs.acs.org/doi/10.1021/acs.est.3c10988.

Information on medium and magnetic measurements, figures showing magnetic characterization, XRD, TEM, high-magnification SEM imaging, SEM-EDXS elemental mapping and size distribution for mineral products, SAED patterns and O K-edge NEXAFS spectra of the FIB cross-section of siderite, and tables with solution chemistry of this study and summary of incubation conditions for DIRB experiments reported in previous studies (PDF)

■ AUTHOR INFORMATION

Corresponding Author

Jinhua Li − *Key Laboratory of Earth and Planetary Physics, Institute of Geology and Geophysics, Chinese Academy of Sciences, Beijing 100029, China; Laboratory for Marine Geology, Qingdao Marine Science and Technology Center, Qingdao 266237, China; College of Earth and Planetary*

https://doi.org/10.1021/acs.est.3c10988
Environ. Sci. Technol. 2024, 58, 11016−11026

Sciences, University of Chinese Academy of Sciences, Beijing 100049, China; orcid.org/0000-0003-1622-6170; Email: lijinhua@mail.iggcas.ac.cn

Authors

Xiaohua Han − *Key Laboratory of Earth and Planetary Physics, Institute of Geology and Geophysics, Chinese Academy of Sciences, Beijing 100029, China; Laboratory for Marine Geology, Qingdao Marine Science and Technology Center, Qingdao 266237, China; Southern Marine Science and Engineering Guangdong Laboratory, Zhuhai 519082, China; College of Earth and Planetary Sciences, University of Chinese Academy of Sciences, Beijing 100049, China;* orcid.org/0000-0003-0305-2706

Fuxian Wang − *Key Laboratory of Earth and Planetary Physics, Institute of Geology and Geophysics, Chinese Academy of Sciences, Beijing 100029, China; Laboratory for Marine Geology, Qingdao Marine Science and Technology Center, Qingdao 266237, China; Southern Marine Science and Engineering Guangdong Laboratory, Zhuhai 519082, China; College of Earth and Planetary Sciences, University of Chinese Academy of Sciences, Beijing 100049, China*

Shiling Zheng − *CAS Key Laboratory of Coastal Environmental Processes and Ecological Remediation, Yantai Institute of Coastal Zone Research, Chinese Academy of Sciences, Yantai, Shandong 264003, China;* orcid.org/0000-0001-9078-6681

Hao Qiu − *Key Laboratory of Earth and Planetary Physics, Institute of Geology and Geophysics, Chinese Academy of Sciences, Beijing 100029, China; Laboratory for Marine Geology, Qingdao Marine Science and Technology Center, Qingdao 266237, China; Southern Marine Science and Engineering Guangdong Laboratory, Zhuhai 519082, China; College of Earth and Planetary Sciences, University of Chinese Academy of Sciences, Beijing 100049, China*

Yan Liu − *Key Laboratory of Earth and Planetary Physics, Institute of Geology and Geophysics, Chinese Academy of Sciences, Beijing 100029, China; Laboratory for Marine Geology, Qingdao Marine Science and Technology Center, Qingdao 266237, China; Southern Marine Science and Engineering Guangdong Laboratory, Zhuhai 519082, China; College of Earth and Planetary Sciences, University of Chinese Academy of Sciences, Beijing 100049, China*

Jian Wang − *Canadian Light Source Inc., University of Saskatchewan, Saskatoon, Saskatchewan S7N 2 V3, Canada*

Nicolas Menguy − *Institut de Minéralogie, de Physique des Matériaux et de Cosmochimie (IMPMC), Sorbonne Université, 75252 Paris Cedex 5, France*

Eric Leroy − *Univ Paris Est Creteil, CNRS, ICMPE, UMR 7182, Thiais F-94320, France*

Julie Bourgon − *Univ Paris Est Creteil, CNRS, ICMPE, UMR 7182, Thiais F-94320, France*

Andreas Kappler − *Geomicrobiology, Department of Geosciences, University of Tübingen, Tübingen 72076, Germany;* orcid.org/0000-0002-3558-9500

Fanghua Liu − *CAS Key Laboratory of Coastal Environmental Processes and Ecological Remediation, Yantai Institute of Coastal Zone Research, Chinese Academy of Sciences, Yantai, Shandong 264003, China; National-Regional Joint Engineering Research Center for Soil Pollution Control and Remediation in South China, Guangdong Key Laboratory of Integrated Agro-Environmental Pollution Control and Management, Institute of Eco-Environmental and Soil Sciences, Guangdong Academy of Sciences, Guangzhou 510650, China*

Yongxin Pan − *Key Laboratory of Earth and Planetary Physics, Institute of Geology and Geophysics, Chinese Academy of Sciences, Beijing 100029, China; College of Earth and Planetary Sciences, University of Chinese Academy of Sciences, Beijing 100049, China*

Complete contact information is available at: https://pubs.acs.org/10.1021/acs.est.3c10988

Author Contributions

[&]X.H. and F.W. are co-first authors.

Notes

The authors declare no competing financial interest.

■ ACKNOWLEDGMENTS

This study was supported financially by the National Natural Science Foundation of China (grants 42225402, 41920104009, 41890843, 42204085, and U20A20109), the Guangdong Foundation for Program of Science and Technology Research (Grant No. 2020B1111530002), the GDAS' Project of Science and Technology Development (Grant No. 2019GDASYL-0102003), and China Postdoctoral Science Foundation (2021M693151). We also thank the TEM and FIB-SEM engineers at the IGG-CAS (Beijing): Mr. Xu Tang and Mr. Lixin Gu for the smooth running of instruments.

■ REFERENCES

(1) Kappler, A.; Bryce, C.; Mansor, M.; Lueder, U.; Byrne, J. M.; Swanner, E. D. An evolving view on biogeochemical cycling of iron. *Nat. Rev. Microbiol.* **2021**, *19* (6), 360−374.

(2) Lovley, D. R.; Ueki, T.; Zhang, T.; Malvankar, N. S.; Shrestha, P. M.; Flanagan, K. A.; Aklujkar, M.; Butler, J. E.; Giloteaux, L.; Rotaru, A.-E.; Holmes, D. E.; Franks, A. E.; Orellana, R.; Risso, C.; Nevin, K. P. Geobacter: The Microbe Electric's Physiology, Ecology, and Practical Applications. *Adv. Microb. Physiol.*; Poole, R. K., Ed.; Academic Press, 2011; vol *59*; pp 1−100.

(3) Fredrickson, J. K.; Zachara, J. M.; Kennedy, D. W.; Dong, H.; Onstott, T. C.; Hinman, N. W.; Li, S. -m. Biogenic iron mineralization accompanying the dissimilatory reduction of hydrous ferric oxide by a groundwater bacterium. *Geochim. Cosmochim. Acta* **1998**, *62* (19), 3239−3257.

(4) Han, X.; Tomaszewski, E. J.; Sorwat, J.; Pan, Y.; Kappler, A.; Byrne, J. M. Effect of Microbial Biomass and Humic Acids on Abiotic and Biotic Magnetite Formation. *Environ. Sci. Technol.* **2020**, *54* (7), 4121−4130.

(5) Lovley, D. R.; Holmes, D. E.; Nevin, K. P. Dissimilatory Fe (III) and Mn (IV) reduction. *Adv. Microb. Physiol.* **2004**, *49*, 219−286.

(6) Jiang, Z.; Shi, M.; Shi, L. Degradation of organic contaminants and steel corrosion by the dissimilatory metal-reducing micro-organisms Shewanella and Geobacter spp. *Int. Biodeterior. Biodegrad.* **2020**, *147*, No. 104842.

(7) Keim, C. N.; Serna, J. D. P.; Acosta-Avalos, D.; Neumann, R.; Silva, A. S.; Jurelevicius, D. A.; Pereira, R. S.; de Souza, P. M.; Seldin, L.; Farina, M. Dissimilatory Iron-Reducing Microorganisms Are Present and Active in the Sediments of the Doce River and Tributaries Impacted by Iron Mine Tailings from the Collapsed Fundão Dam (Mariana, MG, Brazil). *Minerals* **2021**, *11* (3), 244 DOI: 10.3390/min11030244.

(8) Li, J.; Benzerara, K.; Bernard, S.; Beyssac, O. The link between biomineralization and fossilization of bacteria: Insights from field and experimental studies. *Chem. Geol.* **2013**, *359*, 49−69.

(9) Li, J.; Menguy, N.; Leroy, E.; Roberts, A. P.; Liu, P.; Pan, Y. Biomineralization and Magnetism of Uncultured Magnetotactic Coccus Strain THC-1 With Non-chained Magnetosomal Magnetite

Nanoparticles. *J. Geophys. Res.: Solid Earth* **2020**, *125* (12), No. e2020JB020853.
(10) Lee, S. H.; Lee, I.; Roh, Y. Biomineralization of a poorly crystalline Fe (III) oxide, akaganeite, by an anaerobic Fe (III)-reducing bacterium (Shewanella alga) isolated from marine environment. *Geosci. J.* **2003**, *7* (3), 217−226.
(11) Roh, Y.; Zhang, C.-L.; Vali, H.; Lauf, R.; Zhou, J.; Phelps, T. Biogeochemical and environmental factors in Fe biomineralization: magnetite and siderite formation. *Clays Clay Miner.* **2003**, *51* (1), 83−95.
(12) Wu, W.; Li, B.; Hu, J.; Li, J.; Wang, F.; Pan, Y. Iron reduction and magnetite biomineralization mediated by a deep-sea iron-reducing bacterium Shewanella piezotolerans WP3. *J. Geophys. Res.: Biogeosci.* **2011**, *116* (G4), G04034 DOI: 10.1029/2011jg001728.
(13) Lee, J. H.; Roh, Y.; Hur, H. G. Microbial production and characterization of superparamagnetic magnetite nanoparticles by Shewanella sp. HN-41. *J. Microbiol. Biotechnol.* **2008**, *18* (9), 1572.
(14) Wu, W. F.; Wang, F. P.; Li, J. H.; Yang, X. W.; Xiao, X.; Pan, Y. X. Iron reduction and mineralization of deep-sea iron reducing bacterium Shewanella piezotolerans WP3 at elevated hydrostatic pressures. *Geobiology* **2013**, *11* (6), 593−601.
(15) Li, Y.-L. Hexagonal Platelet-like Magnetite as a Biosignature of Thermophilic Iron-Reducing Bacteria and Its Applications to the Exploration of the Modern Deep, Hot Biosphere and the Emergence of Iron-Reducing Bacteria in Early Precambrian Oceans. *Astrobiology* **2012**, *12* (12), 1100−1108.
(16) Vali, H.; Weiss, B.; Li, Y.-L.; Sears, S. K.; Kim, S. S.; Kirschvink, J. L.; Zhang, C. L. Formation of tabular single-domain magnetite induced by Geobacter metallireducens GS-15. *Proc. Natl. Acad. Sci. U. S. A.* **2004**, *101* (46), 16121.
(17) Lu, Y.; Liu, H.; Feng, W.; Xu, Y.; Chen, X. A new and efficient approach for phosphorus recovery from wastewater in the form of vivianite mediated by iron-reducing bacteria. *J. Water Process. Eng.* **2021**, *42*, No. 102200.
(18) Wang, F.; Zheng, S.; Qiu, H.; Cao, C.; Tang, X.; Hao, L.; Liu, F.; Li, J. Ferrihydrite reduction and vivianite biomineralization mediated by iron reducing bacterium Shewanella oneidensis MR-4 [in Chinese with English abstract]. *Acta Microbiol. Sin.* **2018**, *58* (04), 573−583.
(19) Castro, L.; Blázquez, M. L.; González, F.; Muñoz, J. A.; Ballester, A. Heavy metal adsorption using biogenic iron compounds. *Hydrometallurgy* **2018**, *179*, 44−51.
(20) Lee, J.-H.; Roh, Y.; Kim, K.-W.; Hur, H.-G. Organic Acid-Dependent Iron Mineral Formation by a Newly Isolated Iron-Reducing Bacterium, Shewanella sp. HN-41. *Geomicrobiol. J.* **2007**, *24* (1), 31−41.
(21) Sánchez-Román, M.; Fernández-Remolar, D.; Amils, R.; Sánchez-Navas, A.; Schmid, T.; Martin-Uriz, P. S.; Rodríguez, N.; McKenzie, J. A.; Vasconcelos, C. Microbial mediated formation of Fe-carbonate minerals under extreme acidic conditions. *Sci. Rep.* **2014**, *4* (1), 4767.
(22) Dong, H.; Fredrickson, J. K.; Kennedy, D. W.; Zachara, J. M.; Kukkadapu, R. K.; Onstott, T. C. Mineral transformations associated with the microbial reduction of magnetite. *Chem. Geol.* **2000**, *169* (3), 299−318.
(23) Zachara, J. M.; Kukkadapu, R. K.; Fredrickson, J. K.; Gorby, Y. A.; Smith, S. C. Biomineralization of poorly crystalline Fe (III) oxides by dissimilatory metal reducing bacteria (DMRB). *Geosci. J.* **2002**, *19* (2), 179−207.
(24) Dideriksen, K.; Frandsen, C.; Bovet, N.; Wallace, A. F.; Sel, O.; Arbour, T.; Navrotsky, A.; De Yoreo, J. J.; Banfield, J. F. Formation and transformation of a short range ordered iron carbonate precursor. *Geochim. Cosmochim. Acta* **2015**, *164*, 94−109.
(25) Jiang, C. Z.; Tosca, N. J. Fe(II)-carbonate precipitation kinetics and the chemistry of anoxic ferruginous seawater. *Earth Planet. Sci. Lett.* **2019**, *506*, 231−242.
(26) Nealson, K.; Myers, C.; Wimpee, B. Isolation and identification of manganese-reducing bacteria and estimates of microbial Mn (IV)-reducing potential in the Black Sea. *Deep-Sea Res. Part I-Oceanogr. Res. Pap.* **1991**, *38*, S907−S920.
(27) Abd-Aziz, S.; Hung, G. S.; Hassan, M. A.; Karim, M. A.; Samat, N. Indirect method for quantification of cell biomass during solid-state fermentation of palm kernel cake based on protein content. *Asian J. Sci. Res.* **2008**, *1* (4), 385−393.
(28) Stookey, L. L. Ferrozine—a new spectrophotometric reagent for iron. *AnaCh* **1970**, *42* (7), 779−781.
(29) Li, J.; Liu, P.; Menguy, N.; Benzerara, K.; Bai, J.; Zhao, X.; Leroy, E.; Zhang, C.; Zhang, H.; Liu, J.; Zhang, R.; Zhu, K.; Roberts, A. P.; Pan, Y. Identification of sulfate-reducing magnetotactic bacteria via a group-specific 16S rDNA primer and correlative fluorescence and electron microscopy: Strategy for culture-independent study. *Environ. Microbiol.* **2022**, *24* (11), 5019−5038.
(30) Yuan, J.; Su, W.; Hu, X.; Li, X.; Fei, C. Application of Raman imaging and scanning electron microscopy techniques for the advanced characterization of geological samples. *Microsc. Res. Technol.* **2022**, *85* (7), 2729−2739.
(31) Gu, L.; Li, J. The Focused Ion Beam (FIB) Technology and its Applications for Earth and Planetary Sciences [in Chinese with English abstract]. *Bull. Miner. Pet. Geochem.* **2020**, *39*, 1119−1140. +1065−1066.
(32) Li, J.; Menguy, N.; Roberts, A. P.; Gu, L.; Leroy, E.; Bourgon, J.; Yang, X. a.; Zhao, X.; Liu, P.; Changela, H. G.; Pan, Y. Bullet-Shaped Magnetite Biomineralization Within a Magnetotactic Deltaproteobacterium: Implications for Magnetofossil Identification. *J. Geophys. Res.: Biogeosci.* **2020**, *125* (7), No. e2020JG005680.
(33) Wang, J.; Li, J.-H. Scanning transmission x-ray microscopy at the Canadian Light Source: Progress and selected applications in geosciences. *Atom. Spectrosc.* **2022**, *43*, 84−98.
(34) Pan, Y.; Zhu, R.; Banerjee, S. K.; Gill, J.; Williams, Q. Rock magnetic properties related to thermal treatment of siderite: behavior and interpretation. *J. Geophys. Res.* **2000**, *105* (B1), 783−794.
(35) Pan, Y.; Zhu, R.; Liu, Q.; Jackson, M. Low-temperature magnetic behavior related to thermal alteration of siderite. *Geophys. Res. Lett.* **2002**, *29* (23), 2−1−2−4.
(36) Notini, L.; Byrne, J. M.; Tomaszewski, E. J.; Latta, D. E.; Zhou, Z.; Scherer, M. M.; Kappler, A. Mineral Defects Enhance Bioavailability of Goethite toward Microbial Fe(III) Reduction. *Environ. Sci. Technol.* **2019**, *53* (15), 8883−8891.
(37) Byrne, J. M.; Telling, N. D.; Coker, V. S.; Pattrick, R. A. D.; van der Laan, G.; Arenholz, E.; Tuna, F.; Lloyd, J. R. Control of nanoparticle size, reactivity and magnetic properties during the bioproduction of magnetite by Geobacter sulfurreducens. *Nanotechnology* **2011**, *22* (45), No. 455709.
(38) Qu, X.-F.; Yao, Q.-Z.; Zhou, G.-T. Synthesis of siderite microspheres and their transformation to magnetite microspheres. *Eur. J. Mineral.* **2011**, *23* (5), 759−770.
(39) Kniep, R.; Busch, S. Biomimetic growth and self-assembly of fluorapatite aggregates by diffusion in denatured collagen matrices. *Angew. Chem., Int. Ed.* **1996**, *35*, 2624−2626.
(40) Zhou, G. T.; Yao, Q. Z.; Ni, J.; Jin, G. Formation of aragonite mesocrystals and implication for biomineralization. *Am. Mineral.* **2009**, *94*, 293−302.
(41) Qu, X. F.; Yao, Q. Z.; Zhou, G. T.; Fu, S. Q.; Huang, J. L. Formation of hollow magnetite microspheres and their evolution into durian-like architectures. *J. Phys. Chem. C* **2010**, *114*, 8734−8740.
(42) Bourdelle, F.; Benzerara, K.; Beyssac, O.; Cosmidis, J.; Neuville, D. R.; Brown, G. E.; Paineau, E. Quantification of the ferric/ferrous iron ratio in silicates by scanning transmission X-ray microscopy at the Fe L2,3 edges. *Contrib. Mineral. Petrol.* **2013**, *166* (2), 423−434.
(43) Michelin, A.; Drouet, E.; Foy, E.; Dynes, J. J.; Neff, D.; Dillmann, P. Investigation at the nanometre scale on the corrosion mechanisms of archaeological ferrous artefacts by STXM. *J. Anal. At. Spectrom.* **2013**, *28* (1), 59−66.
(44) Koprinarov, I. N.; Hitchcock, A. P.; McCrory, C. T.; Childs, R. F. Quantitative Mapping of Structured Polymeric Systems Using Singular Value Decomposition Analysis of Soft X-ray Images. *J. Phys. Chem. B* **2002**, *106* (21), 5358−5364.

(45) Brandes, J. A.; Wirick, S.; Jacobsen, C. Carbon K-edge spectra of carbonate minerals. *J. Synchrot. Radiat.* **2010**, *17* (5), 676−682.
(46) Brandes, J. A.; Lee, C.; Wakeham, S.; Peterson, M.; Jacobsen, C.; Wirick, S.; Cody, G. Examining marine particulate organic matter at sub-micron scales using scanning transmission X-ray microscopy and carbon X-ray absorption near edge structure spectroscopy. *Mar. Chem.* **2004**, *92* (1), 107−121.
(47) Li, J.; Bernard, S.; Benzerara, K.; Beyssac, O.; Allard, T.; Cosmidis, J.; Moussou, J. Impact of biomineralization on the preservation of microorganisms during fossilization: An experimental perspective. *Earth Planet. Sci. Lett.* **2014**, *400*, 113−122.
(48) Jain, A.; Raven, K. P.; Loeppert, R. H. Arsenite and Arsenate Adsorption on Ferrihydrite: Surface Charge Reduction and Net OH- Release Stoichiometry. *Environ. Sci. Technol.* **1999**, *33* (8), 1179−1184.
(49) Bénézeth, P.; Dandurand, J.; Harrichoury, J. Solubility product of siderite (FeCO3) as a function of temperature (25−250 C). *Chem. Geol.* **2009**, *265* (1−2), 3−12.
(50) Ball, J. W.; Nordstrom, D. K. WATEQ4F--User's manual with revised thermodynamic data base and test cases for calculating speciation of major, trace and redox elements in natural waters. Open-file report, **1991**.
(51) Jiang, C. Z.; Tosca, N. J. Growth kinetics of siderite at 298.15 K and 1 bar. *Geochim. Cosmochim. Acta* **2020**, *274*, 97−117.
(52) Aloisi, G.; Gloter, A.; Krüger, M.; Wallmann, K.; Guyot, F.; Zuddas, P. Nucleation of calcium carbonate on bacterial nanoglobules. *Geology* **2006**, *34* (12), 1017−1020.
(53) Sánchez-Román, M.; Vasconcelos, C.; Schmid, T.; Dittrich, M.; McKenzie, J. A.; Zenobi, R.; Rivadeneyra, M. A. Aerobic microbial dolomite at the nanometer scale: Implications for the geologic record. *Geology* **2008**, *36* (11), 879−882.
(54) Krause, S.; Liebetrau, V.; Gorb, S.; Sánchez-Román, M.; McKenzie, J. A.; Treude, T. Microbial nucleation of Mg-rich dolomite in exopolymeric substances under anoxic modern seawater salinity: New insight into an old enigma. *Geology* **2012**, *40* (7), 587−590.
(55) Cölfen, H.; Qi, L. A Systematic Examination of the Morphogenesis of Calcium Carbonate in the Presence of a Double-Hydrophilic Block Copolymer. *Chem. − Eur. J.* **2001**, *7* (1), 106−116.
(56) Schmahl, W. W.; Griesshaber, E.; Neuser, R.; Lenze, A.; Job, R.; Brand, U. The microstructure of the fibrous layer of terebratulide brachiopod shell calcite. *Eur. J. Mineral.* **2004**, *16* (4), 693−697.
(57) Hansel, C. M.; Benner, S. G.; Fendorf, S. Competing Fe (II)-induced mineralization pathways of ferrihydrite. *Environ. Sci. Technol.* **2005**, *39* (18), 7147−7153.
(58) Heimann, A.; Johnson, C. M.; Beard, B. L.; Valley, J. W.; Roden, E. E.; Spicuzza, M. J.; Beukes, N. J. Fe, C, and O isotope compositions of banded iron formation carbonates demonstrate a major role for dissimilatory iron reduction in ∼ 2.5Ga marine environments. *Earth Planet. Sci. Lett.* **2010**, *294* (1), 8−18.
(59) Isaack, A.; Gischler, E.; Hudson, J. H.; Anselmetti, F. S.; Buhre, S.; Camoin, G. F. Facies variations in response to Holocene sea-level and climate change on Bora Bora, French Polynesia: Unravelling the role of synsedimentary siderite in a tropical marine, mixed carbonate-siliciclastic lagoon. *Mar. Geol.* **2017**, *390*, 1−22.
(60) Wittkop, C.; Teranes, J.; Lubenow, B.; Dean, W. E. Carbon- and oxygen-stable isotopic signatures of methanogenesis, temperature, and water column stratification in Holocene siderite varves. *Chem. Geol.* **2014**, *389*, 153−166.

https://doi.org/10.1021/acs.est.3c10988
Environ. Sci. Technol. 2024, 58, 11016−11026